Multi-scale elastoplastic mechanical model and microstructure damage analysis of solid expandable tubular*

Hui-Juan Guo(郭慧娟)[1,2], Ying-Hua Liu(刘应华)[1], Yi-Nao Su(苏义脑)[2], Quan-Li Zhang(张全立)[2], and Guo-Dong Zhan(詹国栋)[3,†]

[1] *Department of Engineering Mechanics, AML, Tsinghua University, Beijing* 100084, *China*
[2] *Drilling Mechanical Department, CNPC Engineering Technology R & D Company Limited, Beijing* 102206, *China*
[3] *Drilling Technology Division, EXPEC Advanced Research Center, Saudi Arabia*

(Received 27 March 2020; revised manuscript received 10 May 2020; accepted manuscript online 1 August 2020)

We present an in-depth study of the failure phenomenon of solid expandable tubular (SET) due to large expansion ratio in open holes of deep and ultra-deep wells. By examining the post-expansion SET, lots of microcracks are found on the inner surface of SET. Their morphology and parameters such as length and depth are investigated by use of metallographic microscope and scanning electron microscope (SEM). In addition, the Voronoi cell technique is adopted to characterize the multi-phase material microstructure of the SET. By using the anisotropic elastoplastic material constitutive model and macro/microscopic multi-dimensional cross-scale coupled boundary conditions, a sophisticated and multi-scale finite element model (FEM) of the SET is built successfully to simulate the material microstructure damage for different expansion ratios. The microcrack initiation and growth is simulated, and the structural integrity of the SET is discussed. It is concluded that this multi-scale finite element modeling method could effectively predict the elastoplastic deformation and the microscopic damage initiation and evolution of the SET. It is of great significance as a theoretical analysis tool to optimize the selection of appropriate tubular materials and it could be also used to substantially reduce costly failures of expandable tubulars in the field. This numerical analysis is not only beneficial for understanding the damage process of tubular materials but also effectively guides the engineering application of the SET technology.

Keywords: solid expandable tubular (SET), material microstructure damage, multi-scale elastoplastic model, virtual failure

PACS: 46.50.+a, 81.40.Np, 89.30.aj, 91.60.Ed **DOI:** 10.1088/1674-1056/abab6e

1. Introduction

The notion of solid expandable tubular (SET) technology in the oil and gas industry was first proposed by Shell in the late 1990s to trim down the telescopic effect in the casing design as wells were drilled to deeper depths.[1,2] During operation, the SET is preset to the desired position of an oil and gas borehole, an expansion cone is used to cause axial movement by hydraulic or mechanical forces, and the SET expands radially to cause permanent plastic deformation. This allows it to sit closely against the casing or borehole wall so that the desired downhole operation can be accomplished. It can be widely applied in complex drilling and completion processes of horizontal wells and high-angle deviated wells as well as other exceptional wells. The wide application of the SET technology can greatly reduce the drilling cost and shorten the work period.[3,4] At present, the most critical technical problem of the SET is the selection of materials with large expansion ratios. Due to the lack of research and development and the unclear mechanical expansion mechanism of the SET with a large expansion ratio, there is no theoretical basis for the reasonable design and material selection of the SET.[5,6] In particular, a definite expansion ratio limit of the SET material in engineering applications cannot be obtained, which leads to microcrack damage and the loss of structural integrity in the expansion process of the SET.[7–9] However, many studies worldwide are still focused on the calculation of the mesoscale mechanical behaviors due to the material microstructures, lacking cross-scale, and multi-dimensional coupled analyses with macroscopic structure models as well as adequate integration for specific engineering applications and experimental verification.[10–13]

It is a popular interdisciplinary research area in mechanics and materials science currently and an important development direction in this field to study the relationship between the microstructure and macro-properties of materials beginning from the microstructures of the materials.[14] With the development of the basic theory of crystal plastic mechanics, the basic methods of texture analysis, and the experimental and testing means of materials science, researchers and engineers can obtain and analyze information for a growing number of materials (such as the interactions between dislocations, grain boundaries, and grains), which provides new research methods for more accurate predictions and analysis of the plastic deformation and damage behavior of the material

*Project supported by the National Major Science & Technology Project of China (Grant No. 2016ZX05020-003).
†Corresponding author. E-mail: guodong.zhan@aramco.com

microstructure.[15]

Based on the research, development, and application of the SET technology in the petroleum industry, this work focuses on the issue of microcracks present on the inner surface in the expansion process of the SET of a 20G material. The multiphase microstructural features and the surface microcrack morphology were analyzed with a metallographic microscope. The Voronoi algorithm was adopted to generate two-dimensional crystal cells and an axial cross-sectional microstructure digital model of the SET material. Based on this, the simulation analysis of the crystal plastic deformation and damage was realized for the 20G material using a two-phase polycrystal anisotropic elastoplastic large-deformation material constitutive model. The numerical analysis results were consistent with those of the experiments, which can well explain the microscopic damage of the SET and effectively guide engineers to select SET materials with large expansion ratios in the oil industry.

2. Experimental study and failure analysis of SET

2.1. Experimental materials and methods

The experiments in this study were based on the actual engineering problem in which the pressure is too high in the expansion process of the SET operation, resulting in failures during oil/gas field applications in China.[16] Expansion experiments simulating the actual expansion operation were conducted in a laboratory environment at various expansion ratios. Damage and failure analysis was conducted on the SET to better evaluate and analyze the cause of the expansion fracture of the SET and avoid the potential safety hazards in the expansion operation.[17,18]

The SET selected in this paper was a 20G seamless steel tube that is widely used in China. In recent years, with the increasing of 20G SET application, there are more and more failure problems in the field, but these problems have never been detected in the pre-expansion experiments of the laboratory. This is because the indoor tests of SET are all controlled within the limit expansion rate, the apparent rupture of SET never occurred.[19] On the one hand, we make efforts to seek or develop high-performance alternative materials, such as J55, BX80, PZG M65. On the other hand, for consistency with the failure cases in actual engineering projects, we deeply studied the microscopic damage mechanism of 20G material SET. In this paper, a 20G material SET with dimensions of Φ203 mm × 10 mm was used for the expansion tests at the desired expansion ratios of 9.29%, 15.30%, and 17.76%, corresponding to expansion cone diameters of 200, 211, and 215.5 mm, respectively, by the mechanical expansion method.

For the expansion test, the inner surface of the SET was sandblasted, de-rusted, and covered evenly with lubricating grease. The expansion diagram and expansion cone are shown in Fig. 1. The half-cone angle of the expansion cone was 12°, and the friction coefficient was 0.12. Axial pressure was applied to the expansion cone via the pressure head to press the entire expansion cone into the tube and expand the top of the SET.

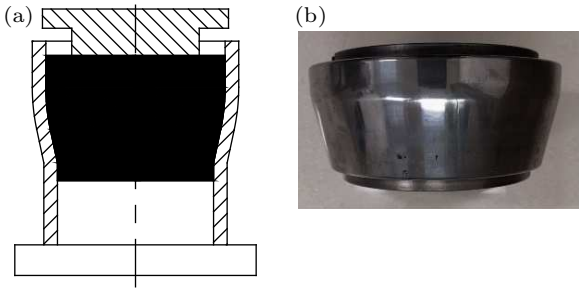

Fig. 1. Mechanical expansion specimen sampling: (a) expansion diagram; (b) expansion cone.

2.2. Test and failure analysis on expandable tubular

2.2.1. Expansion test results and analysis

The sizes and stable expansion pressures of the SET before and after expansion were measured, as shown in Table 1.

Table 1. Geometric dimensions and expansion pressures of 20G SET before and after expansion.

Pre-expansion /mm	Cone *OD*/mm	Expansion ratio/%	Post expansion *ID*/mm	Actual expansion ratio/%	Shorting ratio/%	Wall thickness reduction ratio/%	Expansion pressure/MPa
Φ203 × 10	200	9.29	203.11	11	3.13	6.4	17.8
Φ203 × 10	211	15.30	214.07	16.98	4.54	9.7	24
Φ203 × 10	215.5	17.76	218.53	19.4	5.00	11.1	26.3

In Table 1, expansion ratio $= (OD_{\text{cone}} - ID_{\text{SET}})/ID_{\text{SET}} \times 100\%$, shorting ratio $= (L_{\text{pre}} - L_{\text{post}})/L_{\text{pre}} \times 100\%$, wall thickness reduction ratio $= (T_{\text{pre}} - T_{\text{post}})/T_{\text{pre}} \times 100\%$.

Here, OD_{cone} is the outside diameter of the expansion cone, ID_{SET} is the inside diameter of the SET before expansion. L_{pre} and L_{post} represent the length of the SET before and after expansion, respectively. T_{pre} and T_{post} represent the thickness of the SET before and after expansion, respectively.

As shown in Table 1, after the expansion of the SET, the wall thickness and length decreased, and the actual expansion ratio was not consistent with the design expansion ratio. For example, the design expansion ratio was 15.3%, while the actual expansion ratio was 16.98%. As the expansion ratio increased, the shortening rate of the expandable tubular in-

creased, the wall thickness reduction rate increased, and the corresponding expansion pressure also increased.

2.2.2. Surface crack and damage test analysis

To investigate the root cause of the failures of the expandable tubular in practical engineering applications, SET samples with different expansion ratios of 9.29%, 15.30%, and 17.76% were made and observed for surface crack morphology observations and analysis.

Multiple samples with approximate dimensions of 10 mm ×10 mm×20 mm were cut from the SET before and after the expansion by means of wire cutting. The samples were made as many cold inlaid ones. The surfaces of the samples were burnished and polished with a polishing machine, subsequently cleaned with alcohol and blown dry for later use. The metallographic structures and surface crack morphologies of the inner surfaces, outer surfaces, cross sections, and longitudinal sections of the samples were observed with a LEICA EC3 optical microscope. The sampling, sample preparation, and the viewing direction of the cross section of the test samples are shown in Fig. 2.

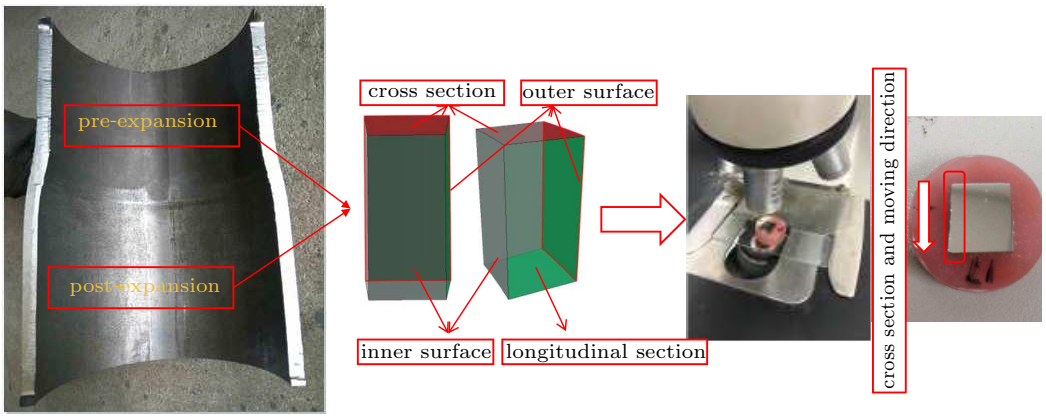

Fig. 2. Sample selection, preparation, and shooting before and after the expansion of SET.

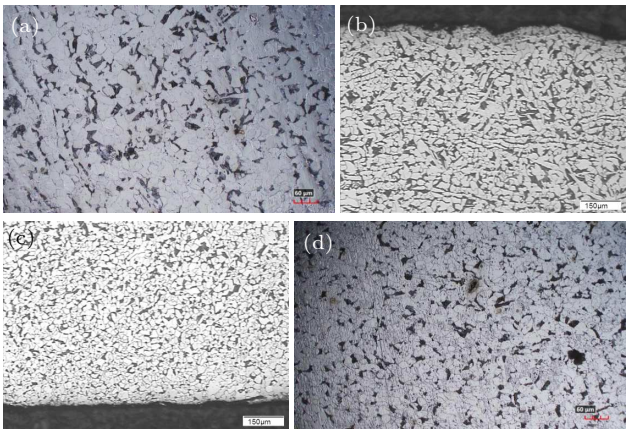

Fig. 3. Metallographic structure and grain size analysis of 20G SET before expansion. (a) Internal surface metallographic structure; (b) metallographic structure of the inner surface of the cross-section; (c) metallographic structure of the external surface of the cross-section; (d) external surface metallographic structure.

Observations were made on the metallographic structure of the 20G SET inner surface, the inner surface of the cross section, the outer surface of the cross section, and the outer surface before expansion. The metallographic structure of the 20G SET was ferrite & pearlite, and the two-phase structure of the interior and exterior surfaces was uniformly distributed. Thereinto, the grain size of the inner surface was about grade 8.0 (Fig. 3(a)), which was slightly lower than that of the outer surface (Fig. 3(d)). The ferrite and pearlite had banded distributions on the inner surface of the cross-section, without an evident decarburized layer (Fig. 3(b)). The ferrite and pearlite were in an approximate isometric crystal distribution on the outer surface of the cross-section, of which the total decarburization was 0.21 mm (Fig. 3(c)).

The metallographic structures and crack morphologies of the inner and outer surfaces of the samples were observed. The inner surfaces with crack defects were ground, and then the crack depths on the inner surfaces of the SET at different expansion ratios were measured. The results showed that no cracks were found on the outer surfaces of the samples after the expansion of the 20G SET at the expansion ratios of 9.29%, 15.30%, and 17.76%. However, many surface microcracks were observed along the direction of 45° on the inner surfaces of the samples. The short and long cracks on the inner surface appeared alternately, the number of short cracks is obviously higher the long one, and the longest crack was about 4 mm. The average crack depths were about 233.0, 272.1, and 310.5 μm at these expansion ratios, respectively. The inner surfaces of the samples were corroded, and all the cracks appeared in two forms: transgranular and intergranular. In order to clearly describe the metallographic structures and crack morphologies of the SET after expansion under different expansion ratios of the internal surfaces, the original picture after cleaning, the metallograph after cutting and corroding, and the corresponding local magnification of microcracks are presented respectively, as shown in Fig. 4.

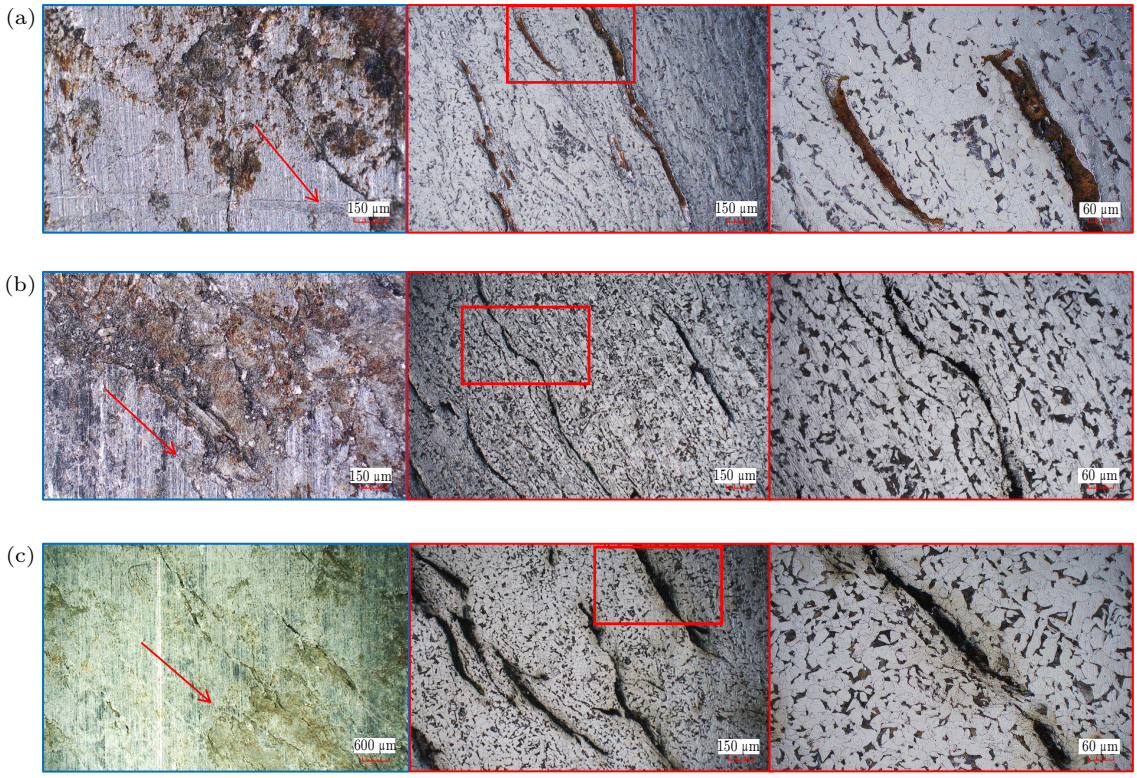

Fig. 4. Metallographic structures and crack morphologies of the expandable tubular after expansion under different expansion ratios and cutting quantities of the internal surfaces. (a) Expansion ratio: 9.29%, cut: 0 μm and 160.0 μm. (b) Expansion ratio: 15.30%, cut: 0 μm and 106.0 μm. (c) Expansion ratio: 17.76%, cut: 0 μm and 200.0 μm

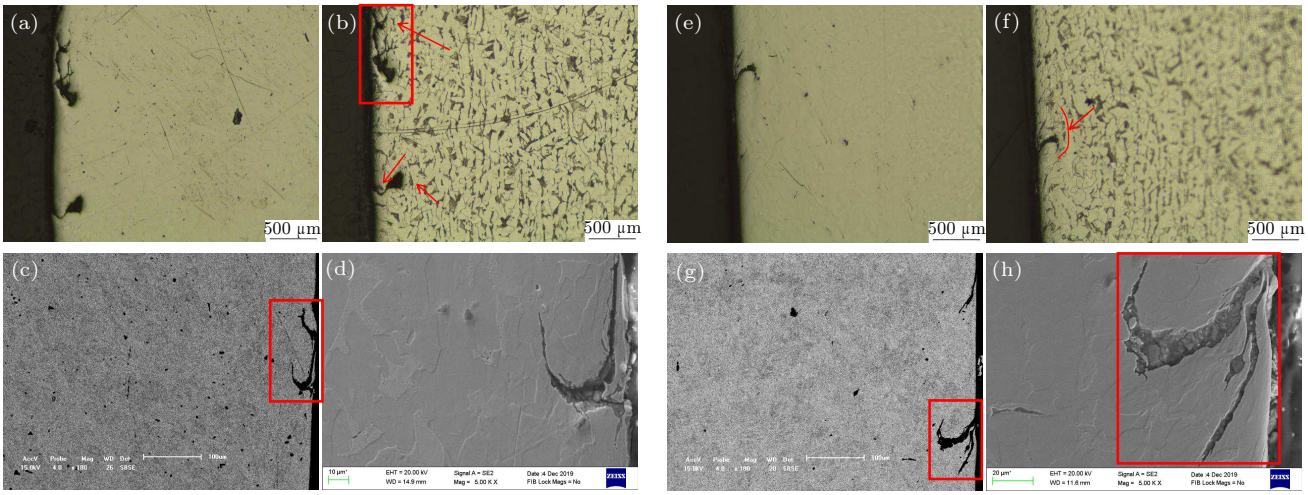

Fig. 5. Metallographic, backscatter, and secondary electron scanning images of post-expansion SET at the expansion ratio of 17.76%. (a) Metallography of the uncorroded cross-section; (b) metallography of the corroded cross-section; (c) cross-sectional backscatter scanning image; (d) cross-sectional secondary electron scanning image; (e) metallography of the uncorroded longitudinal section; (f) metallography of the corroded longitudinal section; (g) longitudinal-sectional backscatter scanning image; (h) longitudinal-sectional secondary electron scanning image.

To further study the initiation mechanism of the microcracks on the 20G SET, cracks in the same location were marked, and the microcracks and crack tips on the cross and longitudinal sections of the SET samples for an expansion ratio of 17.76% were observed with an optical microscope and scanning electron microscope (SEM) in backscattered electron mode and secondary electron scanning. The crack morphologies were analyzed and compared, as shown in Fig. 5.

The surfaces of the test samples were corroded using 4% nitric acid and alcohol. The surfaces of the samples were cleaned with distilled water and blown dry for use. The sample surfaces were observed with a SHIMADZU SS-550 scanning electron microscope in backscattered electron mode, and the accelerating voltage was 15.0 kV. In addition, to enhance the conductivities of the samples, the cold inlaid sample block was sprayed with gold for 15 s. After gold spraying, the samples were placed on Petri dishes for later use. A Zeiss Auriga focused ion beam and field-emission double-beam scanning electron microscope was used to observe the surfaces of the samples, and the acceleration voltage was 20.00 kV.

The results showed that about ten microcracks were distributed on the upper surface of the 10-mm-long cross-section, two of which were selected, as shown in Figs. 5(a)–5(d). About six microcracks were distributed on the surface of the 20-mm long longitudinal section, and one of them was selected, as shown in Figs. 5(e)–5(h). The propagation directions of the surface cracks on both sections exhibited certain inclination angles, and the deepest crack on the upper and longitudinal section was about 600 μm. The results of the backscattering and secondary electron scanning showed that the cracks typically initiated inside the tube near the surface and propagated along the outer diameter and axial direction. When the crack propagation path met a concentrated pearlite with banded zone, the crack propagated along the extending direction of the zone until it broke through the zone and underwent transgranular or intergranular propagation into the ferrite structure. This showed that crack propagation typically avoided the pearlitic phase with a higher intensity and hardness and chose paths with lower fracture energies. In addition, crack bifurcation during propagation is another manifestation of damage mechanism.

3. Elastoplastic mechanical model and numerical simulation of SET

3.1. Elastoplastic structural FEM of SET

To determine the failure cause of SET from the mechanical model, this study adopted the finite element software Simulia Abaqus to perform numerical simulations on the deformation process of SET.[10] Based on the characteristics of the expansion deformation, the elastoplastic mechanical analysis was performed with a two-dimensional (2D) axisymmetric model and a full three-dimensional (3D) structure model, respectively. By comparing the model and analysis results, the structural damage, which might be caused by the structural deformation, plastic strain, and residual stress in the deformation process, was analyzed.

The structure models of the expansion cone and the 20G material SET in the model were consistent with those of the experiments. The cone was modeled as a discrete rigid body with an outer diameter of 220 mm and cone angle of 12°. The deformable expandable tubular had a diameter of Φ203 mm, thickness of 10 mm, and the length of 300 mm. Based on the measured stress-strain relationship of the 20G material, the elastoplastic material constitutive model was adopted, the material parameters of the SET before expansion were set (as shown in Table 2), and the geometric nonlinear analysis was defined. In the model, by defining the axial displacement of the expansion cone as 420 mm, the mechanical expansion molding process of the test was simulated, and the thrust of the expansion cone in the test was calibrated by outputting the reaction force.

The characteristic size of the elements of the axisymmetric and three-dimensional solid structure model of the SET was 2.0 mm. The 2D axisymmetric model of the expandable tubular contained 906 nodes and 750 four-node bilinear axisymmetric reduced integration quadrilateral elements (CAX4R), and the three-dimensional solid structure model of the expandable tubular contained 1.212×10^5 nodes and 1.0×10^5 eight-node linear reduced integration elements (C3D8R). The finite element model of the expansion process is shown in Fig. 6.

Table 2. Mechanical properties of the pre-expansion and post-expansion 20G tubular.

	Yield strength $R_p0.2$/MPa	Tensile strength R_m/MPa	Elongation A/%	Reduction of area Z/%	Modulus of elasticity/GPa
Pre-expansion	290–310	460–470	35–37	61.5–62.5	206–208
Post-expansion	450–470	560–570	15–17	56–58.8	209–212

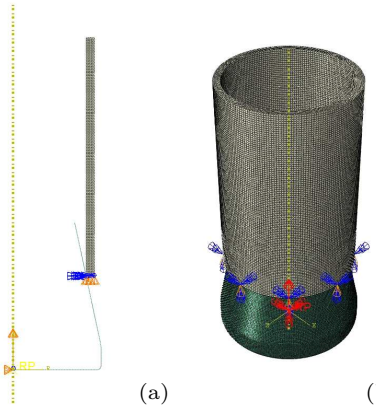

Fig. 6. Finite element model of expansion process. (a) Axisymmetric structure model; (b) complete 3D structure model.

3.2. Analysis and comparison of results

In order to describe the stress state and residual stress distribution of the SET during the expansion process, the equivalent stress (MISES) diagram and the principal stress vector diagram were generated for the 2D axisymmetric model of the SET when the expansion cone moved to the middle of the SET. The results showed that the extreme value of MISES was 577.0 MPa, located at the position of the inner and outer tube walls in the region where the maximum contact force between the cone and the SET. This position moved along the axial direction with the advance of the expansion cone, as shown in Fig. 7(a). The maximum value of MISES was composed of the annular tensile stress of the SET and the local compres-

sive stress of the expansion cone and tube wall, as shown in Fig. 7(b). In addition, by comparing the stress analysis results of the axisymmetric and 3D structure models of the expandable tubular, it was shown that the MISES extreme values were fully consistent with the distribution of the stress field variables.

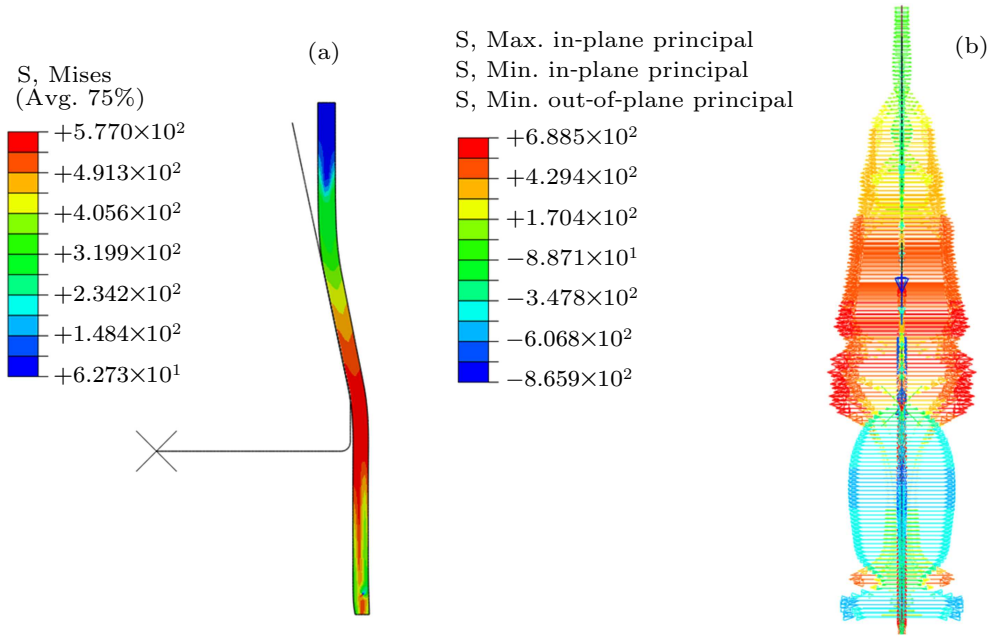

Fig. 7. Stress field variables of axisymmetric model of the SET. (a) MISES diagram; (b) principal stress vector diagram.

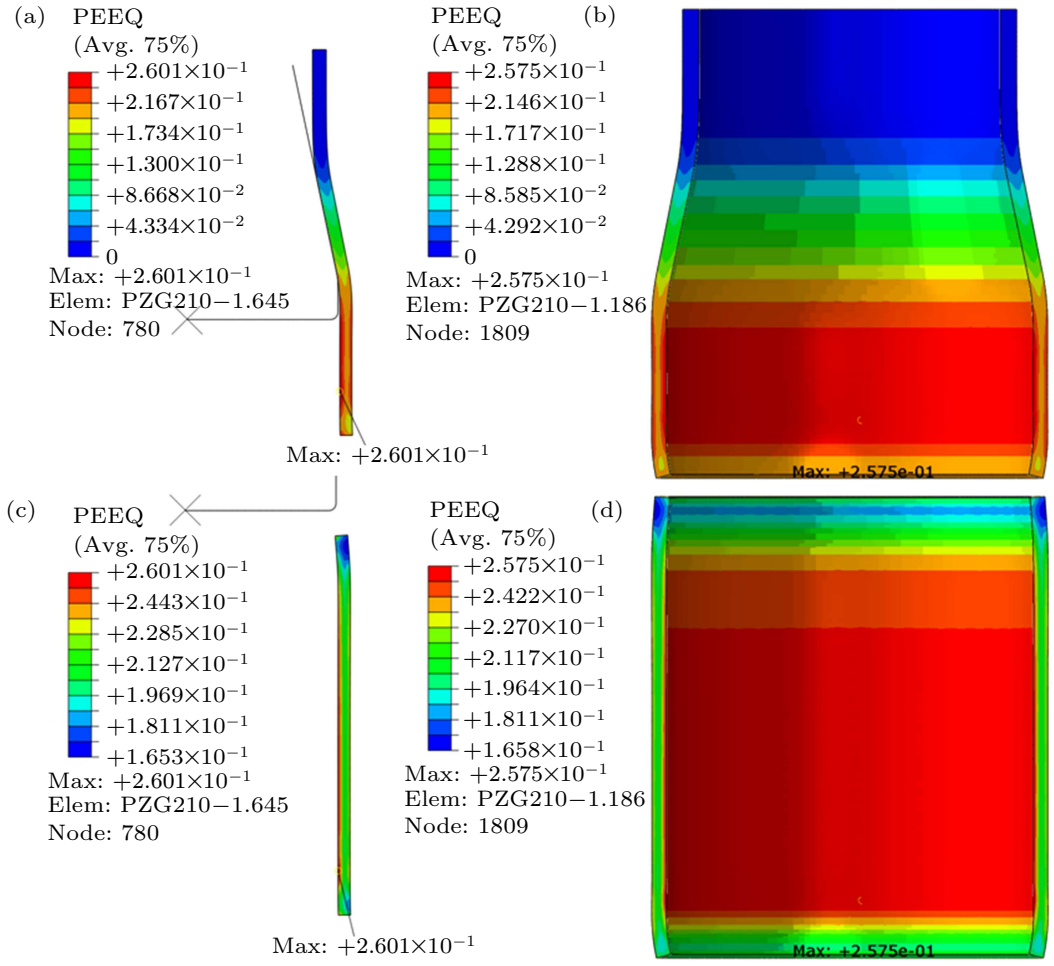

Fig. 8. Accumulated plastic strain PEEQ diagram of the two models of the SET. (a) PEEQ diagram of the axisymmetric model at intermediate time point; (b) PEEQ diagram of the 3D structure model at the intermediate time point; (c) PEEQ diagram of the axisymmetric model at the final time point; (d) PEEQ diagram of the 3D structure model at the final time point.

The accumulated equivalent plastic strain (PEEQ) values were generated and compared for the 2D axisymmetric model and 3D structure model at different analysis moments. The results showed that the corresponding distribution of PEEQ were basically the same for the two kinds of model at the same time points as shown in Figs. 8(a)–8(d). The PEEQ value of the inner surface was 0.2601 in the 2D axisymmetric model, which was slightly higher than the PEEQ value of 0.2575 in the 3D structure model. The results of this analysis were consistent with material plastic yield strength theory (the second strength theory). Thus, the PEEQ of the SET would first cause plastic damage on the inner surface, and the surface microcracks initiation and propagation occur gradually. As the rate of expansion increases, cracks will penetrate the SET. Therefore, when the limit expansion rate is reached, the SET ruptures.

The diagrams of the contact pressure and contact status of the inner surface of the 3D structure model were obtained, as shown in Fig. 9. The results showed that the maximum contact pressure occurred at the root of the reduced section of the expansion cone, and the maximum contact pressure was 585.0 MPa, as shown in Fig. 9(a). The initial and root reduced section positions of the SET showed approximately linear contact states, and the reduced region in the middle showed a surface contact status, as shown in Fig. 9(b).

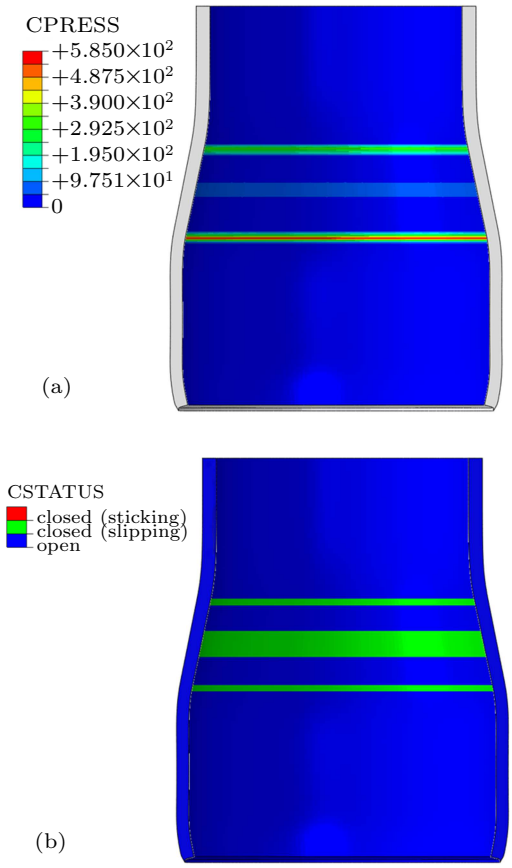

Fig. 9. Contact forces on the inner surface of the 3D structure model of the SET. (a) Diagram of contact pressure; (b) diagram of contact status.

To verify the accuracy of the analysis results, the curves of the reaction force (RF) and the displacement of the expansion cone in the axisymmetric and 3D structure models were generated and compared, as shown in Fig. 10. The results showed that the numerical simulation results of the two models were basically identical. The expansion cone showed stress mutation at the time of size reduction to enter and exit the SET. The phenomenon was caused by the metal plastic resilience of the SET. It is important to have reasonable control over the plastic deformation on both ends of the SET to guarantee the rate of the finished products and the service life of SET in the engineering applications.

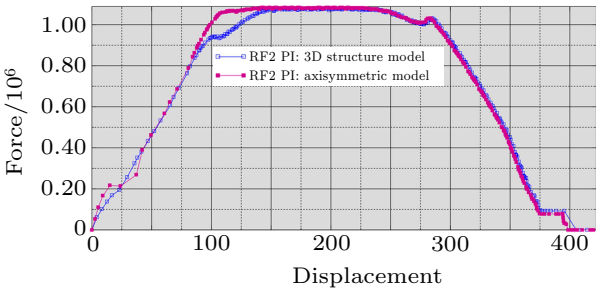

Fig. 10. Comparison of the relationship curves of the reaction force (RF) and displacement of the expansion cone in the 2D axisymmetric model and 3D structure model.

The expansion process of the SET was analyzed based on the two finite element models. Uniform equivalent stress and accumulated plasticity appeared on the inner surface of the SET. Thus, the model failed to provide a good description of the metallography and the microcrack initiation on the inner surface of the SET in the SEM test, even if the material plastic damage constitutive model or increased expansion ratios were considered in the macrostructure model. Therefore, to find and characterize the inner surface damage of the SET, it is necessary to introduce the material microstructure and crystal plastic deformation and damage methods in the simulation to simulate the initiation and propagation process of microcracks on the inner surface of the SET.

4. Multi-scale model and numerical simulation of SET

4.1. Multi-scale material microstructure FEM of SET

4.1.1. Two-phase heterogeneous microstructure characterization of SET

To numerically simulate the microstructure crystal plasticity and damage of the SET, in this paper, based on the Voronoi algorithm, we independently developed the representative volume element (RVE) of the multi-component and heterogeneous material microstructures using VC++ programming and the OpenGL toolset.[14] The microstructure of the two-phase heterogeneous material was established for the 20G SET. The finite element mesh division, crystallographic orientation definition, material constitutive model parameter set-

ting, macro-microscopic boundary condition coupled models, and numerical calculation of the micromechanics were achieved through secondary development of the commercial finite element software ABAQUS. In addition, to achieve accurate and efficient numerical analysis of the material microstructure of the SET and reduce the computational cost, material microstructural models were built using 2D Voronoi polygons to characterize the upper sections on the inner surface elements. Consequently, the axial cross section of the minimum hexahedral element was consistent with the size of the RVE boundary or was an equal-proportion structure model. In order to solve the differences in scale and the numerical error problem between the macroscopical model of the SET and the model of two-phase material microstructure, that is, for example, 1-mm structural feature of the SET is a huge size for the material microstructure model, if the same system of units "mm" are used in FEM modeling, the minimum characteristic size of grain in the microstructure model may be in the order of 10^{-6} mm, which have certain unfavorable effects on the numerical accuracy obviously. Therefore, in the modeling process, we enlarged the scale of the microstructure by 1000 times, and achieved the consistency of its numerical solution through the constraint system of units. Moreover, by transforming the "μm" units of the microstructure model into "mm" units of the 3D macroscopic structure model, the numerical accuracy of the polygon vertices and other problems in the Voronoi graphs were eliminated. Figure 11 shows that the coupled boundary conditions of the macro-microscopic model for the microstructure of the SET material.

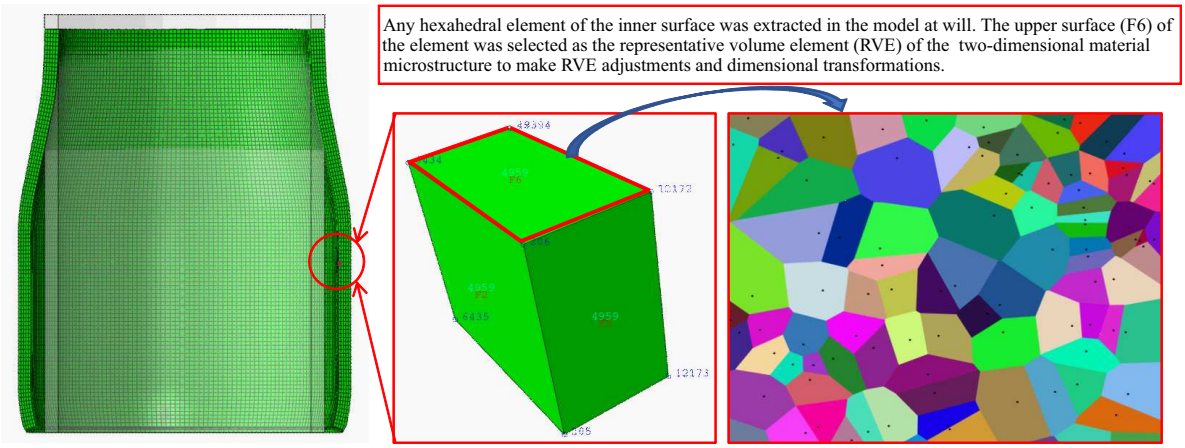

Fig. 11. Coupling diagram of boundary conditions of the macro-micromodel for the microstructures of the SET.

Based on the construction of the material microstructural model of the Voronoi algorithm, the planar space was divided into many element regions.[20,21] The spatial Voronoi diagram was defined as follows.

(i) Given the set S of n points in a 3D Euclidean space, $S = \{p_1,\ p_2,\ \ldots,\ p_n\} \subset R_3$, $d(S,P_i)$ was the Euclidean distance between S and P_i.

(ii) The space division given by $V_n(P_i) = \cap j \neq I\{S \in R_3 | d(S,P_i) < d(S,P_j)\}$ was called the Voronoi diagram with set $S = \{p_1,\ p_2,\ \ldots,\ p_n\} \subset R_3$ as the space point set, denoted as $V_{\mathrm{or}}(S)$.

(iii) $V(P_i)$ $(i = 1,2,\ldots,n)$ was a Voronoi polyhedron, referred to as a Voronoi cell, and P_i $(i = 1,2,\ldots,n)$ was called the generator of a Voronoi cell.

Common algorithms for constructing Voronoi diagrams include incremental algorithms, divide-and-conquer algorithms, decremental algorithms, and the plane-sweep algorithm. Among them, the incremental algorithm is not only applicable to the static point set but also suitable for dynamic point sets, and thus, it has attracted extensive attention. In this paper, this algorithm was adopted. Its time complexity is $O(n2)$. By adding random points one by one and making local modifications to the geometrical information data, the complete Voronoi diagram was constructed. To effectively control the geometrical morphology of the RVE of the polycrystalline matrix, the method for adjusting the average grain size in a given area was adopted, namely, after the volume mean of the volumes of different areas relative to the cell number in a given representative element was obtained, the equivalent spherical radius equal to the volume mean was taken as the average grain size in the region. By adjusting the parameters of the average sizes of the grains in different regions of the representative volume element and giving the spatial coordinates of the initial Voronoi cell generator at random, the geometric morphology of the representative volume element of the multi-component and heterogeneous material was finally determined. Based on the metallographic structure of the 20G SET, the characteristics of the element section of the complete 3D structure model, and the polycrystalline material microstructure RVE of the average grain size of approximately 30 μm containing 5000 grains, the microstructural distribution of ferrite and pearlite was simulated by selecting grain sets in different areas and

layers. The final constructed two-phase heterogeneous material microstructure model of the SET (the light gray grains are ferrite and the dark black ones are pearlite) is shown in Fig. 12.

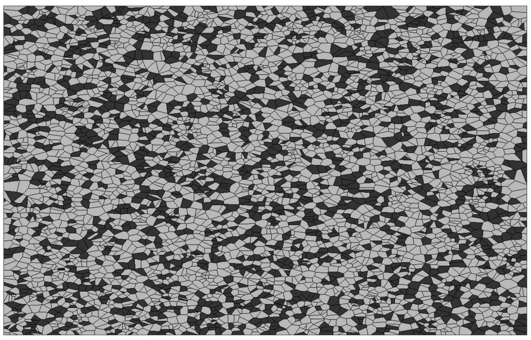

Fig. 12. Microstructural model of the two-phase heterogeneous material of the SET.

4.1.2. Elastoplastic and damage constitutive model of material microstructure

Crystallographic anisotropy is the core features of the material microstructural constitutive model. It is an anisotropic behavior caused by the different orientations, the irregular geometrical shape, the non-uniform distribution of material component, in addition, produced by the inhomogeneity of the mesoscopic stress field in the material microstructure. The anisotropy of the two-phase heterogeneous microstructure can also be characterized by the crystallographic orientation.[22,23]

Normally, the orientation of the crystal requires a reference coordinate system to adjust a set of axes to determine the rotation of the lattice (or, conversely, to adjust the coordinate system to determine the lattice axes). In Euler space $\Omega(\theta,\Phi,\Psi\in\Omega)$ three angles (polar angle θ, azimuth angle Ψ, and rotation angle Φ) are defined, they are used to describe the spatial orientation of grain. Figure 13(a) shows the arbitrary orientation of a grain. For the i-th arbitrarily oriented grain, the local coordinates $(\alpha_i,\beta_i,\gamma_i)$ can be related to the reference coordinate system (α,β,γ) by the following expression:

$$\begin{pmatrix}\cos\alpha_i\\ \cos\beta_i\\ \cos\gamma_i\end{pmatrix}=R(\theta,\psi,\phi)\begin{pmatrix}\cos\alpha\\ \cos\beta\\ \cos\gamma\end{pmatrix}, \tag{1}$$

Here, R is the transformation matrix associated with the three angles in Euler space

$$R(\theta,\psi,\phi)=\begin{pmatrix}A & B & -\sin\theta\cos\phi\\ C & D & \sin\theta\sin\phi\\ \sin\theta\cos\psi & \sin\theta\sin\psi & \cos\theta\end{pmatrix}. \tag{2}$$

Here,

$$\begin{aligned}A&=\cos\theta\cos\psi\cos\phi-\sin\psi\sin\phi,\\ B&=\cos\theta\sin\psi\cos\phi+\cos\psi\sin\phi,\\ C&=-\cos\theta\cos\psi\sin\phi-\sin\psi\cos\phi,\\ D&=-\cos\theta\sin\psi\sin\phi+\cos\psi\cos\phi.\end{aligned}$$

In Euler space $\Omega(\theta,\Phi,\Psi\in\Omega)$, $\theta\in(0,\pi)$, $\Phi\in(0,2\pi)$, $\Psi\in(0,2\pi)$. By use of a series of coordinate transformations, the crystallographic orientation of a grain can be described by a set of spatial coordinates in the global coordinate system.

The main feature of the heterogeneous material microstructure model is that each grain in the multi-grain set is assumed to be an anisotropic continuum with different orientations.[24,25] The linear anisotropic elastic formula is given by Hooke's law

$$\sigma_{ij}=D_{ijkl}\varepsilon_{kl}. \tag{3}$$

Here, σ_{ij} represents the second order stress tensor matrix, D_{ijkl} represents the fourth order stiffness matrix, ε_{kl} represents the second-order strain tensor matrix. In the application, nine independent linear stiffness matrix parameters are used to define the material microstructure as orthotropic linear elasticity.

$$\begin{Bmatrix}\sigma_{11}\\ \sigma_{22}\\ \sigma_{33}\\ \sigma_{12}\\ \sigma_{13}\\ \sigma_{23}\end{Bmatrix}=\begin{bmatrix}D_{1111} & D_{1122} & D_{1133} & 0 & 0 & 0\\ & D_{2222} & D_{2233} & & & \\ & & D_{3333} & & & \\ & & & D_{1212} & & \\ & \text{sym} & & & D_{1313} & \\ & & & & & D_{2323}\end{bmatrix}=\begin{Bmatrix}\varepsilon_{11}\\ \varepsilon_{22}\\ \varepsilon_{33}\\ \varepsilon_{12}\\ \varepsilon_{13}\\ \varepsilon_{23}\end{Bmatrix}=\left[D^{\mathrm{el}}\right]\begin{Bmatrix}\varepsilon_{11}\\ \varepsilon_{22}\\ \varepsilon_{33}\\ \varepsilon_{12}\\ \varepsilon_{13}\\ \varepsilon_{23}\end{Bmatrix}. \tag{4}$$

The basic assumption of the elastic–plastic model of materials is that deformation can be divided into elastic parts and inelastic (plastic) parts.[26] Its general form is

$$F=F^{\mathrm{el}}F^{\mathrm{pl}}. \tag{5}$$

Here, F is the total deformation gradient, F^{el} is the fully recoverable deformation at the point of integration, F^{pl} is the plastic permanent deformation.

For the elastic-plastic model, it is usually necessary to consider the strain rate correlation, and the strain rate can be decomposed into

$$\dot{\varepsilon}=\dot{\varepsilon}^{\mathrm{el}}+\dot{\varepsilon}^{\mathrm{pl}}. \tag{6}$$

Here, $\dot{\varepsilon}$ is the total strain rate, $\dot{\varepsilon}^{\mathrm{el}}$ is the elastic strain rate, $\dot{\varepsilon}^{\mathrm{pl}}$ is the plastic strain rate.

Two rate-dependent models are usually considered for

plastic deformation. One is the introduction of rate-dependent yield strength into the material model to solve relatively high strain rate applications, such as dynamic events or metal forming process simulation. The other is the introduction of the power law.

$$\dot{\bar{\varepsilon}}^{\mathrm{pl}} = D\left(\frac{\bar{\sigma}}{\sigma^0} - 1\right)^n \quad \text{for} \quad \bar{\varepsilon} \geq \sigma^0. \tag{7}$$

Here, $\dot{\bar{\varepsilon}}^{\mathrm{pl}}$ is the equivalent plastic strain rate, $\bar{\sigma}$ is the yield stress at the non-zero plastic strain rate, $\sigma^0\left(\varepsilon^{\mathrm{pl}}, \theta, f_i\right)$ is the static yield stress with the plastic strain, temperature, field variables.

The initiation and evolution of plastic damage are mainly caused by failure mechanisms: the ductile failure caused by the nucleation, growth, and merger of micropores, and the shear failure caused by the localization of shear zone. Based on the phenomenological study of material constitutive model, the two mechanisms require the different damage initiation criteria.[27,28]

The ductile criterion is a phenomenological model for predicting damage caused by nucleation, growth, and coalescence of pores. The model assumes that the equivalent plastic strain $\bar{\varepsilon}_{\mathrm{D}}^{\mathrm{pl}}$ at the beginning of the damage is a function of the triaxial stress and strain rate, that is $\bar{\varepsilon}_{\mathrm{D}}^{\mathrm{pl}}(\eta, \dot{\bar{\varepsilon}}^{\mathrm{pl}})$. $\eta = -p/q$ is the triaxial stress, p is the compressive stress, q is the Mises stress, $\dot{\bar{\varepsilon}}^{\mathrm{pl}}$ is the equivalent plastic strain rate, and the conditions that meet the damage initiation criteria are as follows:

$$\omega_{\mathrm{D}} = \int \frac{\mathrm{d}\bar{\varepsilon}^{\mathrm{pl}}}{\bar{\varepsilon}_{\mathrm{D}}^{\mathrm{pl}}(\eta, \dot{\bar{\varepsilon}}^{\mathrm{pl}})} = 1. \tag{8}$$

Here, ω_{D} is the state variable that increases monotonically with plastic deformation. In the analysis process, the following conditions shall be met for each incremental calculation:

$$\Delta\omega_{\mathrm{D}} = \frac{\Delta\bar{\varepsilon}^{\mathrm{pl}}}{\bar{\varepsilon}_{\mathrm{D}}^{\mathrm{pl}}(\eta, \dot{\bar{\varepsilon}}^{\mathrm{pl}})} \geq 0. \tag{9}$$

The latest experimental results show that besides the stress triaxiality and strain rate, ductile fracture can also depend on the third invariant of deviating stress, which is related to the Lord's angle (or pole angle). The equivalent plastic strain $\bar{\varepsilon}_{\mathrm{D}}^{\mathrm{pl}}$ at the beginning of ductile damage, as a function of the Lode angle, $\bar{\varepsilon}_{\mathrm{D}}^{\mathrm{pl}}(\eta, \xi(\Theta), \dot{\bar{\varepsilon}}^{\mathrm{pl}})$,

$$\xi(\Theta) = \cos(3\Theta) = \left(\frac{r}{q}\right)^3. \tag{10}$$

Here, q is the Mises stress, and r is the third invariant of the partial stress. The value of this function, $\xi(\Theta)$, ranges from the stress state of the compressed meridian, $\xi = -1$, to the stress state of the stretched meridian, $\xi = 1$.

The shear criterion is a phenomenological model for predicting the onset of localized damage in shear bands. The model assumes that the equivalent plastic strain, $\bar{\varepsilon}_{\mathrm{S}}^{\mathrm{pl}}$, at the beginning of damage is a function of the shear stress ratio and strain rate, $\bar{\varepsilon}_{\mathrm{S}}^{\mathrm{pl}}(\theta_{\mathrm{s}}, \dot{\bar{\varepsilon}}^{\mathrm{pl}})$. Here, $\theta_{\mathrm{s}} = (q + k_{\mathrm{s}}p)/\tau_{\max}$ is the shear stress ratio, $\tau_{\max}$ is the maximum shear stress, and k_{s} is the material parameter. When the following conditions are met, the criterion for the initiation of shear damage is satisfied.

$$\omega_{\mathrm{S}} = \int \frac{\mathrm{d}\bar{\varepsilon}^{\mathrm{pl}}}{\bar{\varepsilon}_{\mathrm{S}}^{\mathrm{pl}}(\theta_{\mathrm{s}}, \dot{\bar{\varepsilon}}^{\mathrm{pl}})} = 1. \tag{11}$$

Here, ω_{S} is the state variable that increases monotonically with plastic deformation and is proportional to the incremental change of the equivalent plastic strain. In the analysis process, the following conditions will be met for each incremental calculation:

$$\Delta\omega_{\mathrm{S}} = \frac{\Delta\bar{\varepsilon}^{\mathrm{pl}}}{\bar{\varepsilon}_{\mathrm{S}}^{\mathrm{pl}}(\theta_{\mathrm{s}}, \dot{\bar{\varepsilon}}^{\mathrm{pl}})} \geq 0. \tag{12}$$

Figure 13(b) describes the characteristic stress–strain behavior of materials undergoing damage. In hardened elasto-plastic materials, damage usually takes two forms: yield stress softening and elastic degradation. In the figure, the solid curve represents the stress–strain response to material damage, while the dotted line represents the response to nondestructive damage. As described later, the damage response is largely dependent on cell size to minimize the resulting grid dependency. In the figure, σ_{y0} and $\bar{\varepsilon}_0^{\mathrm{pl}}$ are the yield stress and equivalent plastic strain at the beginning of the damage, and $\bar{\varepsilon}_{\mathrm{f}}^{\mathrm{pl}}$ is the equivalent plastic strain at the failure, that is, when the overall damage variable $D = 1$ reaches this value. Overall damage variable D captures the comprehensive effect of all active damage mechanisms and is calculated according to the weight of each damage variable d_i.

When the material fails, the equivalent plastic strain value, $\bar{\varepsilon}_{\mathrm{f}}^{\mathrm{pl}}$, depends on the characteristic length of the element, and cannot be used as a material parameter to describe the damage evolution law. On the contrary, the damage evolution law is defined by equivalent plastic displacement $\bar{u}^{\mathrm{pl}}$ or fracture energy dissipation G_{f}. When a material damaged, the stress–strain relationship no longer accurately represents the behavior of the material. A strong grid dependence based on strain localization is introduced by continuing to use the stress–strain relationship, so that the dissipated energy decreases with the refinement of the grid. To realize the stress-displacement concept in the finite element model, the characteristic length L associated with the integral point is defined. Then, the fracture energy is expressed as

$$G_{\mathrm{f}} = \int_{\bar{\varepsilon}_0^{\mathrm{pl}}}^{\bar{\varepsilon}_{\mathrm{f}}^{\mathrm{pl}}} L\sigma_{\mathrm{y}}\,\mathrm{d}\bar{\varepsilon}^{\mathrm{pl}} = \int_0^{\bar{\varepsilon}_{\mathrm{f}}^{\mathrm{pl}}} L\sigma_{\mathrm{y}}\,\mathrm{d}\bar{u}_{\mathrm{f}}^{\mathrm{pl}}. \tag{13}$$

The expression introduces the definition of equivalent plastic displacement, $\bar{u}^{\mathrm{pl}}$, as the fracture work conjugate (crack

work per unit area) of the yield stress after the onset of damage. $\dot{\tilde{u}}^{\mathrm{pl}} = 0$ before the onset of damage, $\dot{\tilde{u}}^{\mathrm{pl}} = L\dot{\tilde{\varepsilon}}^{\mathrm{pl}}$ after the damage starts.

$$d_{\mathrm{mult}} = 1 - \prod_{k \in N_{\mathrm{mult}}} (1 - d_k). \tag{14}$$

The total damage variable is calculated as the maximum value of the damage variable, d_{mult}, and the residual damage variable, $D = \max\left\{d_{\mathrm{mult}}, \max_{j \in N_{\mathrm{mult}}} (d_j)\right\}$. Here, N_{mult} and N_{max} represent the set of activation mechanisms that contribute to overall damage in the multiplicative and maximum sense, respectively, that is $N_{\mathrm{act}} = N_{\mathrm{mult}} \cup N_{\mathrm{max}}$.

To assign orientation information to the grains of the two-phase heterogeneous material microstructure, in this study, a random number generator was used to generate the information data for the two kinds of Euler angles (polar angle θ, azimuth Ψ, and rotation angle Φ) of the random distribution and specific statistical distribution. The specific statistical distributions included a normal distribution, exponential distribution, and gamma distribution. The grain and phase structure were defined as different element sets and assigned with the crystallographic orientation of the material. In the microstructure of 20G material, pearlite is a mechanical mixture composed of alternating ferrite and cementite lamellae. There are many studies on the anisotropic linear elastic material parameters of cementite and ferrite. In this study, refer to the relevant references,[29,30] the orthotropic elastic stiffness of the two-phase material microstructure is determined, as shown in Table 3. According to experimental data and relevant studies, monocrystal elastoplastic material data were defined for the cementite and ferrite. The yield strength and ultimate strength of cementite are much greater than those of ferrite. Therefore, for defining a constitutive model, only the material plastic model data were considered for cementite, while the elastoplasticity and toughness–shear damage and the damage evolution parameters based on the fracture energy density were considered for the matrix ferrite materials.

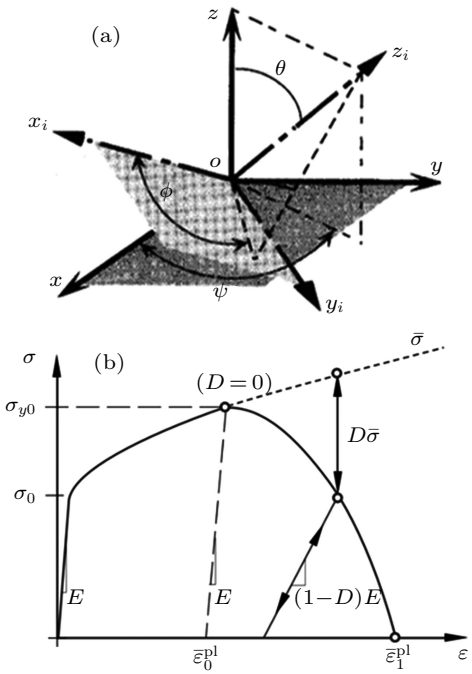

Fig. 13. Microstructure material constitutive model of expansion tube: (a) grain anisotropy of two-phase heterogeneous body and (b) elastoplasticity and damage model.

Table 3. Orthotropic elastic stiffness of the two-phase heterogeneous microstructure of expandable tubulars.

Component	D1111	D2222	D3333	D1122	D1133	D2233	D1212	D1313	D2323	μ[a]	λ[a]
Ferrite	265.6	166.2	259.8	111.6	117.9	117.3	84.2	84.8	77.7	69.8	97.2
Cementite	394.0	350.0	322.0	159.0	163.0	164.0	19.0	133.0	133.0	227.0	252.0

[a]Lamé constants, $\mu = C_{44} - (2C_{44} + C_{12} - C_{11})/5$ and $\lambda = C_{12} - (2C_{44} + C_{12} - C_{11})/5$.

4.2. Results of numerical analysis of material microstructure model

To describe the mechanical behavior of the axial cross section of the SET, the mesh of the material microstructure model contained a first-order plane strain reduction integral element consisting of 86386 quadrilaterals mixed with 6902 triangles, and the number of mesh nodes was 90387. The element deformation corresponding to the expansion rate 17.76% of the macroscopic SET model is applied to the upper surface section. The numerical analysis results of the microstructure of the two-phase heterogeneous material of the SET were finally obtained by parallel calculations.

The overall model of material microstructure, MISES diagram, and PEEQ diagram of the ferrite matrix phase and pearlite second phase were output, as shown in Fig. 13. The results showed that due to the crystallographic anisotropy and the elastoplastic differences of two-phase structure, there was a significant stress gradient in the entire model. The stress level of pearlite phase was significantly higher than that of ferritic phase, and the stress range was about 49.4 MPa–1350 MPa, as shown in Fig. 14(a). Thus, the two-phase polycrystalline material reached the yield state. In addition, the stress levels of different grains in the single-phase structure were significantly different. The stress range of ferritic phase was 49.4 MPa–577.0 MPa, as shown in Fig. 14(b) and that of pearlite phase was 91.7 MPa–1350 MPa, as shown in Fig. 14(c). The analysis results showed that the inner surface of the larger boundary displacement deformation of the material microstructure had a significant accumulated plastic strain PEEQ gradient. The large strain direction was in good agree-

ment with the direction of crack initiation and propagation. Thus, the PEEQ field variables were the comprehensive analysis indices that reflected the two-phase microstructure damage and determined the final state of the virtual failure of the microstructure, as shown in Fig. 14(d).

Since the material damage model of the ferrite matrix phase of the two-phase heterogeneous material microstructure of SET was considered, the stiffness decline degree (SDEG) of the ferrite phase and the automatic failure element removal function could be characterized in the post-treatment analysis, as shown in Fig. 15(a). From the comparison between the numerical analysis results and the metallographic test ones, we can find that in the RVE about three microcracks mainly initiate at the interface position of the ferritic matrix phase and pearlite, and the microcracks propagated on the inner surface of the microstructure along the direction of the least resistance in the ferritic matrix phase or along the interface of the two phases. When the expansion deformation is applied to the upper surface section of microstructure, the average length of the three cracks reaches about 8 element characteristic lengths, *i.e.*, about 240 μm. The longest microcrack is about 280 μm, slightly lower than the average crack length observed in the experiment, which was 300 μm. The crack initiation and propagation morphology were basically identical with the experimental results, as shown in Fig. 15(b).

To further identify the cause of the microstructure failure, the multiple damage initial criterion, and the evolution process, the diagrams of the ductile damage initial criterion (DUCTCRT) and the shear damage initial criterion (SHRCRT) of the material microstructure were output, as shown in Fig. 16. The analysis results showed that the initiation of all the microcracks occurred in the regions where the stiffness values of the two kinds of materials reached 1, which occurred mainly at the grain boundary of the two-phase heterogeneous material. The region of toughness damage was relatively significant. In addition to the distribution on the edge of the surface of the microstructure, the initial criterion for the toughness damage was also reached in a large area in the internal region, as shown in Fig. 16(a). In contrast, shear damage was mainly concentrated at the surface edge of the microstructure, especially at the crack initiation area or the leading edge. Therefore, shear damage had a more significant effect on the initiation and propagation of microcracks, which was mainly caused by the crystal slippage generated by the ferrite phase at the two-phase interface of the microstructure, as shown in Fig. 16(b).

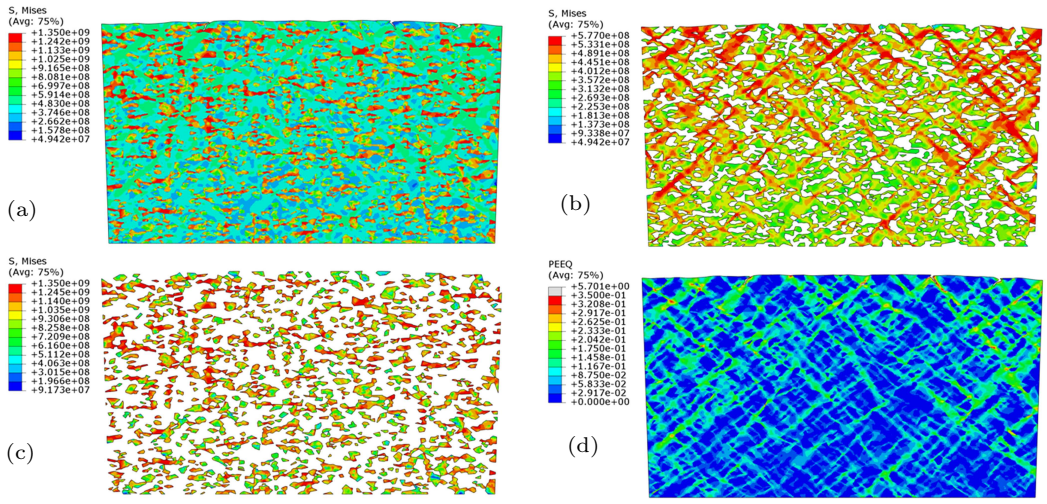

Fig. 14. Stress and strain field distribution results of virtual failure analysis of microstructure. (a) Overall MISES diagram; (b) MISES diagram of ferrite matrix phase; (c) MISES diagram of pearlite second phase; (d) Overall PEEQ diagram.

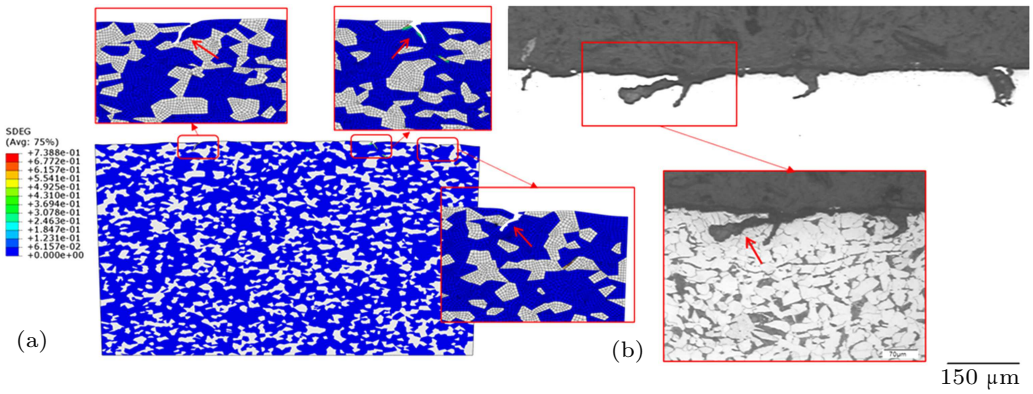

Fig. 15. Comparison of virtual failure analysis results of the microstructure from the numerical calculations and test results. (a) Stiffness decline degree of virtual failure (SDEG) diagram; (b) Analysis results of metallographic test.

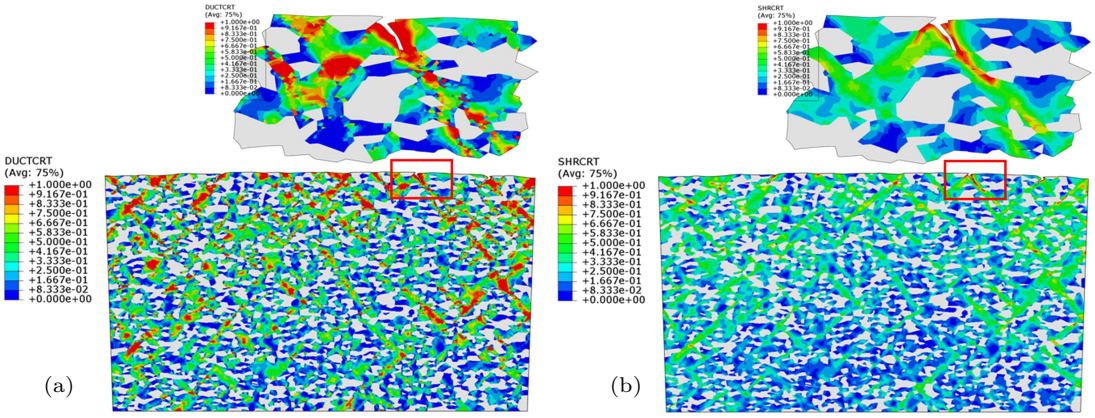

Fig. 16. Diagram of damage initial criterion and evolution. (a) Ductile damage initial criterion (DUCTCRT) diagram; (b) shear damage initial criterion (SHRCRT) diagram.

5. Conclusion and perspectives

In view of the damage and rupture problems of the SET in drilling and completion operations, an in-depth study was conducted on the damage mechanisms and virtual failure behaviors of 20G SET at different expansion ratios by means of experiments and numerical simulations. The crystal plasticity and damage simulation analysis of the two-phase heterogeneous material microstructure of the SET was also presented. The following conclusions were reached.

i) The crack initiation occurred inside the SET near the surface and propagated along the outer diameter and axial direction, the microcracks distributed along the 45° direction, and the cracks appeared in two forms, transgranular and intergranular.

ii) The main cause of the inner surface failure of the SET was annular tensile stress. However, the uniform equivalent stress and accumulated plasticity that appeared on the inner surface failed to explain the initiation and propagation of the microcracks on the inner surface of the SET in the metallographic tests.

iii) The sizes and morphologies of the microcracks that initiated along the inner surface of the microstructure and the two-phase structural interface in the cross-scale simulation were basically consistent with the test results.

The 2D Voronoi polygons model cannot fully reflect the plastic deformation and damage evolution process of the two-phase structure. Therefore, it is necessary to develop a complete 3D finite element model for the three-phase heterogeneous material microstructure of the SET for further in-depth analysis of the problem.

References

[1] Cales G L 2003 *The development and applications of solid expandable tubular technology, Canadian International Petroleum Conference*, 10–12 June, 2003, Calgary, Alberta, Canada, p. 136

[2] Shao C 2015 *Petrochem. Ind. Technol.* **22** 152 (in Chinese)

[3] Zhang J, Shi T and Lian Z 2003 *China Petrol. Mach.* **31** 128 (in Chinese)

[4] Zhang J and Zhao H 2015 *Oil and Gas Well Expansion Tube Technology* (Beijing: Petroleum Industry Press) p. 47 (in Chinese)

[5] Wei F, Bi Z Y, Li Y Z, Tang J, Wang T and Su W 2014 *Steel Pipe* **43** 34 (in Chinese)

[6] Shen W Z 2013 *Study and development of the new expandable tubular ferrite/martensite dual phase steels*, Ph. D. Dissertation (Chengdu: Southwest Petroleum University) (in Chinese)

[7] Pervez T 2010 *J. Achiev. Mater. Manuf. Eng.* **41** 147

[8] Li X, Dou F, Pei Y and Li D 2005 *Oil Field Equip.* **34** 61 (in Chinese)

[9] Al-Abri O S and Pervez T 2013 *Int. J. Solids Struct.* **50** 2980

[10] Pervez T and Qamar S Z 2011 *Adv. Mater. Res.* **264** 1654

[11] Pervez T, Seibi A C and Karrech A. 2005 *J. Petrol. Sci. Technol.* **23** 775

[12] Seibi A C, Al-Hiddabi S and Pervez T 2005 *J. Energy Resour. Technol.* **127** 323

[13] Pervez T, Seibi A C and Karrech A 2005 *Pet. Sci. Technol.* **23** 775

[14] Ren H H, Li X D 2009 *Acta Phys. Sin.* **58** 4041 (in Chinese)

[15] Roters F, Eisenlohr P, Hantcherli L, Tjahjanto D D, Bieler T R and Raabe D 2010 *Acta Mater.* **58** 1152

[16] Liao X, Qi Y, Zhu X, Cheng F, Fu D, Shi C, Huang M and Qin F 2019 *Eng. Fail. Anal.* **106** 104135

[17] Pervez T, Qamar S Z, Al-Abri O S and Khan R 2012 *Mater. Manuf. Processes* **27** 727

[18] Ghosh A and Gurao N P 2016 *Mater. Design* **109** 186

[19] Tiwari S, Mishra S, Odeshi A, Szpunar J A and Chopkar M 2017 *Mater. Sci. Eng.* **683** 94

[20] Feng L, Jia B B, Zhu C S, An G S, Xiao R Z and Feng X J 2017 *Chin. Phys. B* **26** 080504

[21] Moghaddam M G, Achuthan A, Bednarcyk B A, Arnold S M and Pineda E J 2017 *Mater. Sci. Eng.* **703** 521

[22] Nguyen T, Luscher D J and Wilkerson J W 2017 *J. Mech. Phys. Solids* **108** 1

[23] Peng H, Pei X Y, Li P, He H L and Bai J S 2015 *Acta Phys. Sin.* **64** 216201 (in Chinese)

[24] Ma Y Q and Zhou Y K 2015 *Chin. Phys. B* **24** 030204

[25] Guo X Q, Wu P D, Wang H, Mao X B and Neale K W 2016 *Int. J. Solids Struct.* **90** 12

[26] Shen W, Fan Q B, Wang F C and Ma Z 2013 *Chin. Phys. B* **22** 044601

[27] Kim D J, Bae K D, Lee H S, Kim Y J and Park G C 2016 *Proced. Struct. Integr.* **2** 825

[28] He R, Wang M T, Jin J F and Zong Y P 2017 *Chin. Phys. B* **26** 128201

[29] Xu W, Wu H, Ma H and Shan D 2017 *Int. J. Mech. Sci.* **135** 226

[30] Cortese L, Nalli F and Rossi M 2016 *Int. J. Plast.* **85** 77